Fundamental Understanding of Interface Chemistry and Electrical Contact Properties of Bi and MoS₂

Seong Yeoul Kim¹, Zheng Sun², Joy Roy¹, Xinglu Wang¹, Zhihong Chen², Joerg Appenzeller² and Robert M. Wallace¹*

¹ Department of Materials Science and Engineering, The University of Texas at Dallas, Richardson, TX 75080, United States of America

² School of Electrical and Computer Engineering and Birck Nanotechnology Center, Purdue University, West Lafayette, Indiana 47907, United States

KEYWORDS: transition metal dichalcogenides, two-dimensional semiconductor, semimetal contact, interface chemistry, band alignment, Fermi level

ABSTRACT

The interface properties and thermal stability of bismuth (Bi) contacts on molybdenum disulfide (MoS₂) shed light on their behavior under various deposition conditions and temperatures. The

examination involves extensive techniques, including X-ray Photoelectron Spectroscopy (XPS), Scanning Tunneling Microscopy (STM), and Scanning Tunneling Spectroscopy (STS). Bi contacts formed a van der Waals (vdW) interface on MoS₂ regardless of deposition conditions, such as ultra-high vacuum (UHV, 3×10⁻¹¹ mbar) and high vacuum (HV, 4×10⁻⁶ mbar), while the oxidation on MoS₂ has been observed. However, the semi-metallic properties of Bi suppress the impact of defect states, including oxidized-MoS₂ and vacancies. Notably, the n-type characteristic of Bi/MoS₂ remains unaffected, and no significant changes in the Local Density of States (LDOS) near the Conduction Band Minimum (CBM) are observed despite the presence of defects detected by STM and STS. As a result, the Fermi Level (E_F) resides below the conduction band of MoS₂. The study also examines the impact of annealing on the contact interface, revealing no interface reaction between Bi and MoS₂ up to 300 °C. These findings enhance our understanding of semimetal (Bi) contacts on MoS₂, with implications for improving the performance and reliability of electronic devices.

Introduction

Molybdenum disulfide (MoS₂) is a representative transition metal dichalcogenides (TMD) material that has received considerable research focus in recent years due to its remarkable mechanical, electronic, and optoelectronic properties. MoS₂ has demonstrated promising electronic device performance, such as a near-ideal subthreshold swing (~60 mV/dec), high I_{on}/I_{off} ratio (>10⁶), and mobility (~200 cm²V⁻¹s⁻¹).¹⁻⁴ However, there are still unsolved problems regarding the intrinsic performances of opto- and electronic devices.⁵ In particular, contact resistance is a crucial issue that has been studied from various perspectives. Notably, the Schottky

barrier height between contact metal and channel TMD materials does not always align with the traditional Schottky-Mott theory, which typically defines the Schottky barrier height the difference between metal contact work function and the Fermi level of semiconductor. 6-12 The possible reasons for these inconsistencies are considered to underestimate the impacts of fabrication conditions and process methods. 13,14 The metal-induced gap state (MIGS) originates from the penetration of the metal's electronic wavefunctions into the band gap of the semiconductor. 15 This influences where the Fermi level becomes "pinned" within the band gap. 16 Moreover, defectinduced gap states (DIGS) are also known as determining the electrical contact properties at the interface, which can determine the conductance type of semiconductor due to defects rather than the contact metal's work function. 12,17 Recently, semimetal contacts have been suggested to avoid the Fermi level pinning problem by suppressing MIGS and DIGS, and they have been reported to have low contact resistance with high on-current density. ^{16,18,19} It appears that work functions (Sn: 4.38 eV, Bi: 4.25 eV, Sb: 4.01 eV)²⁰ close to the conduction band minimum of MoS₂, and the density of states (DOS) saturates to zero where the Fermi level resides. This alignment plays a significant role in achieving these excellent n-type contact properties. In addition, the thermal stability of the contact interface assumes a significant role in metal contacts on Transition Metal Dichalcogenides (TMD) due to the annealing process inherent in semiconductor fabrication. During the back end of line (BEOL) fabrication, the annealing process reaches temperatures up to 400 °C.^{21,22} Consequently, a comprehensive understanding of interface properties under different temperature conditions, up to 400 °C or lower, becomes imperative.

To comprehensively understand the contact properties, it is important to investigate the interface chemistry and determine the role of interfacial chemistry, defects, MIGS, and the deposition ambient with apparent device performance. In this work, XPS is employed to reveal the contact interface reaction and the resulting band alignment between Bi and MoS₂, offering a macroscopic view of the interface. Additionally, STM and STS are used to provide detailed insights at the atomic scale between MoS₂ and Bi, both with and without the presence of defects.

Results

Interface chemistry

In the Bi/MoS₂ bulk system, the formation of strong interface bonding between Bi and MoS₂ is found to be below the detection limit, regardless of the deposition ambient, as shown in Figure 1. This observation implies that MoS₂ maintains its surface crystal structure without undergoing a substantial reaction to the presence of Bi. Concerning the chemical state of MoS₂, the full width at half maximum (FWHM) of the Mo 3d peak is initially measured to be 0.53 eV before metal deposition. Subsequently, the FWHMs after deposition are recorded at 0.49 eV (UHV) and 0.57 eV (HV), respectively. Notably, these FWHM changes fall within 0.05 eV, the energy resolution of the hemispherical analyzer of the monochromatic XPS, indicating that the insignificant changes in the chemical bonding state are below the limit of detection. The FWHMs of the S 2p peaks corresponding to MoS₂ states are detailed in Table S1 for both HV and UHV conditions before and after Bi deposition, indicating no detectable change in the chemical state. These findings are consistent with thermodynamic predictions by the Gibbs free energy, where $\Delta G^{\circ}_{f,MoS_2}$ (-112.95 kJ/mol) is lower than $\Delta G^{\circ}_{f,Bi_2S_3}$ (-46.87 kJ/mol).²⁰

In the Mo 3*d* spectra of the HV-Bi/MoS₂ system presented in Figure 1(a), the presence of MoO_x bonding features is evident at a binding energy (BE) around 230 eV (orange peak fit), while MoO₃ feature, between 232.1 to 233.6 eV²³, is below the detection limit of XPS. In addition, oxidation

of the Bi to form Bi₂O₃ bonding is also detected (BE = 159.2 eV, Figure 1(b)). Such oxidation may be attributed to the water and -OH residues in the HV chamber or the subsequent exposure to air during the *ex-situ* transfer process, potentially leading to the surface oxidation of bulk-MoS₂. Oxidation is plausible when considering that the activation energy barrier can be overcome, particularly given the thermodynamically favorable bonding states of MoO₂ ($\Delta G^{\circ}_{f,MoO_2}$ =-226.50 kJ/mol) and MoO₃ ($\Delta G^{\circ}_{f,MoO_3}$ =-266.67 kJ/mol). The XPS analysis for the detection of such oxidation is noted in the S 2*p* spectra, as shown in Figure 1(b), with detailed zoomed-in peak fitting results in Figure 1(c).

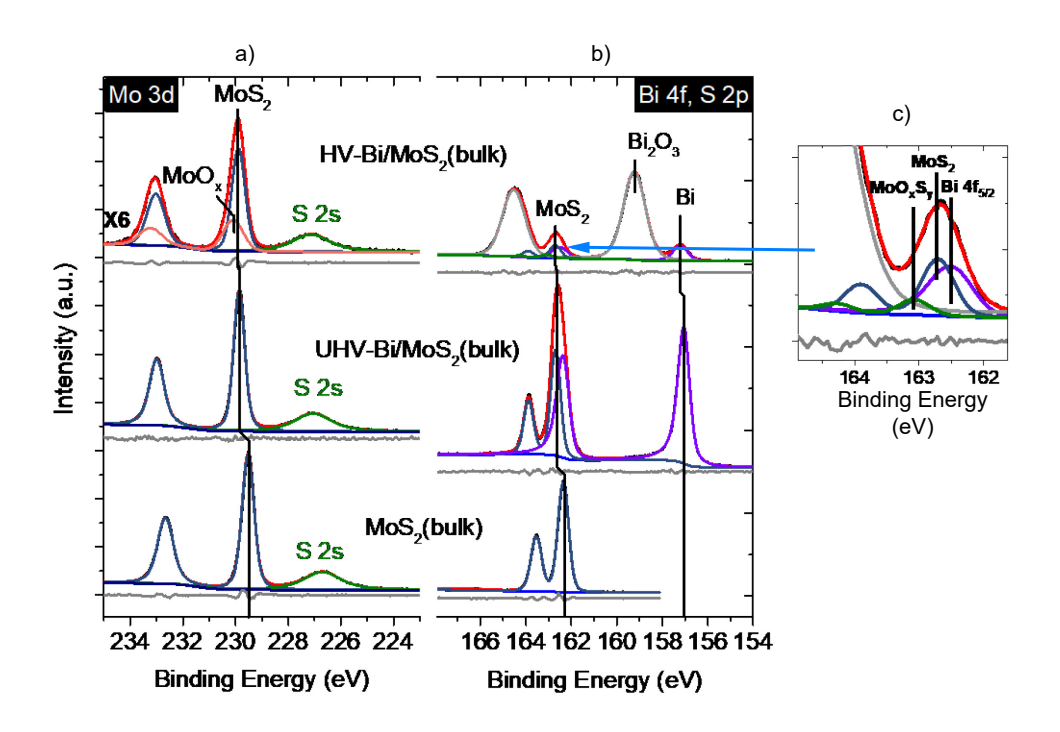


Figure 1 (a) Mo 3d, (b) Bi 4f and S 2p XPS reference spectra of the freshly exfoliated bulk-MoS₂ sample, the bottom spectra are before metal deposition, and the spectra are after UHV and HV metal deposition. (c) Zoomed-in XPS BE region 165.0-161.5 eV after HV-Bi deposition. The y-axis of spectra was not normalized, but the HV metal deposition sample was multiplied 6 times to

show the evolution of spectra while the process progressed. The residuals of the peak fitting are plotted underneath spectra as a gray curve.

The O 1s and C 1s spectra also exhibit no discernible reaction products with MoS₂ or Bi, as shown in Figure 2(a, b). The O 1s core level spectra of the HV-Bi sample in Figure 2(a) show that reasonable oxide features are attributed to adventitious carbon/organic compounds and oxidized Bi (Bi₂O₃) resulting from the *ex-situ* transfer process. However, the Mo-O bonding feature falls below the detection limit of XPS when examining the O 1s core levels. It's important to note that the sensitivity factor (0.711) for O 1s is smaller than that for Mo 3d (2.867), and overlapping oxide features further complicate their distinction. In Figure 2(b), the presence of adventitious carbon species (C-C, C-O, and C=O) is evident, likely originating from the brief exposure of the sample to air during the transition from exfoliation to placement within the cluster tool. Nevertheless, the detection of carbon reaction products bonded with Bi and MoS₂ (with a BE region 282.0-283.2 eV labeled as "M-C") remains below the limits of detection for XPS.

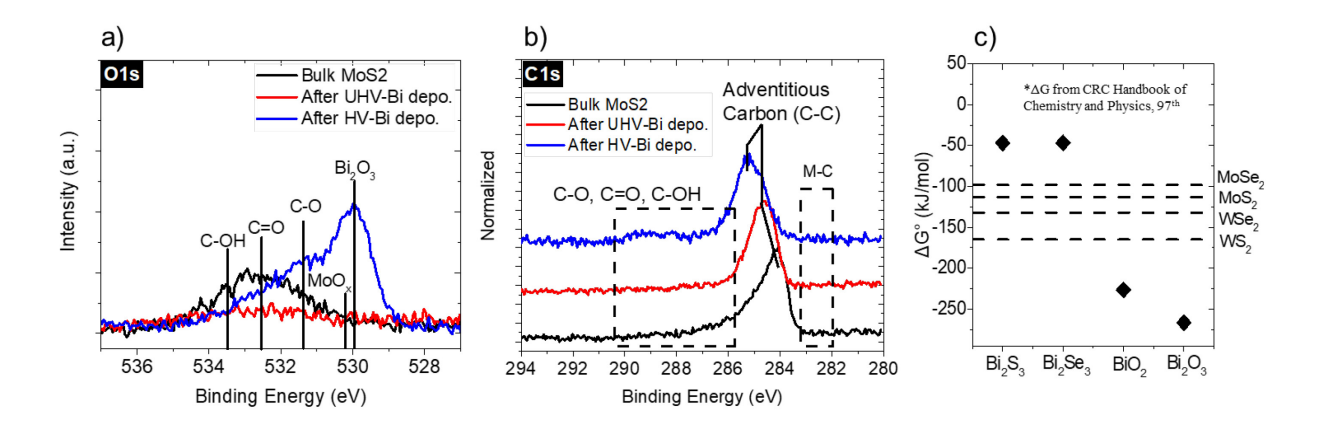


Figure 2 (a) O 1s, and (b) C 1s XPS spectra of the bulk-MoS₂ sample before and after Bi deposition under UHV and HV conditions, (c) The Gibbs free energy plot of the possible interface reaction products between TMD materials and Bi.

The surface morphology, as revealed by *ex-situ* AFM scanning, demonstrates the formation of islands on bulk-MoS₂ following Bi deposition, as depicted in Figure 3. These findings are consistent with the Volmer-Weber growth model, which elucidates island growth due to a weak interaction between Bi/MoS₂ and is corroborated by the XPS results. While the quartz crystal microbalance (QCM) indicated an equivalent Bi thickness of 1 nm across the unit surface area, the ex-situ AFM revealed that the actual average thickness of the Bi islands reached 2.4 nm. It is important to note that this measurement reflects Bi oxidation due to the ex-situ AFM process, as shown in Figure S2, meaning that the XPS data includes information from the contact interface. Furthermore, Supporting Information Section 2 illustrates that oxidation can occur during the *ex-situ* transfer process through the exposed MoS₂ surface. In Figure S2, we identified distinguishable features like MoS₂, MoO_xS_y, and S-O bonding by analyzing oxidized Mo characteristics corresponding to the previously reported.²⁴ These results indicate that long-term air exposure can

partially lead to oxidation, specifically MoO_xS_y and S-O. Considering the HV sample's relatively short air exposure time, it becomes challenging to disregard the potential occurrence of oxidation during the HV e-beam deposition for Bi contact on bulk-MoS₂ under typical device fabrication conditions.

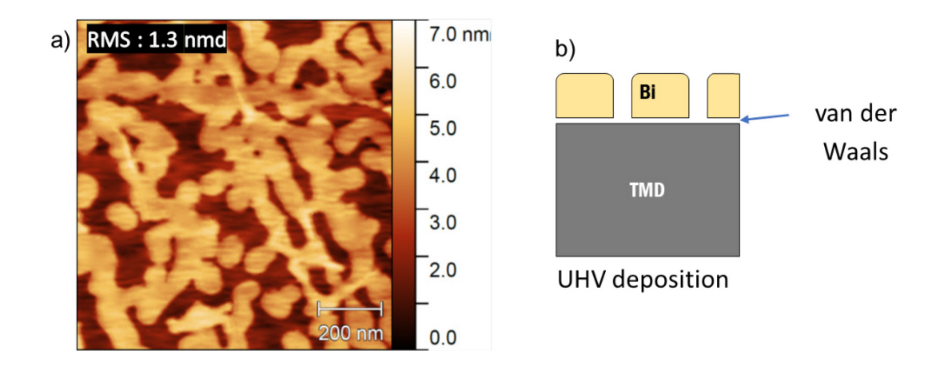


Figure 3 (a) The AFM surface morphology analysis after UHV-Bi deposition. (b) The schematic side-view draw after Bi deposition.

Device performance of (UHV and HV) Bi contact on 1L-MoS₂ field-effect transistors

The contact resistance of 1L-MoS2 field-effect transistors (FET) reveals a dependence on the deposition ambient for the same contact metal, as reported in several studies for other contact metals on TMDs.^{25–28} This dependency is partially attributed to the degradation of metal properties caused by the specific conditions of the deposition ambient, demonstrating sensitivity to both the deposition ambient and the fabrication process for MoS₂-based electrical devices. Despite this, MoS₂ field-effect transistors exhibit commendable device performance irrespective of the Bi deposition ambient. The Experimental Methods section below provides details on the device fabrication.

Figure 4 shows the transfer and output characteristics of Bi contacted 1L-MoS₂ FETs, deposited at different vacuum conditions. Figure 4(a) presents a set of HV-Bi contacted 1L-MoS₂ FETs with different channel lengths. A clear channel length dependent I_{DS} is observed. A similar behavior also is observed at UHV-Bi contacted ML MoS₂ FETs, as shown in Figure 4(b). Because the thickness of dielectric layers is different between HV-Bi and UHV-Bi contacted ML MoS₂ FETs, we compare the output curves of HV-Bi and UHV-Bi at a similar carrier density in Figure 4(c). The carrier density is calculated from the dielectric layer and air gap between 1L-MoS₂ and the dielectric layer²⁹. As shown in Figure 4(c), the HV-Bi and UHV-Bi contacted 1L-MoS₂ FETs present a similar current level in the output curves. After the contact resistance extraction through the Transfer Length Method (TLM) structure of HV-Bi and UHV-Bi contacted ML MoS₂ FETs,³⁰ we plot the contact resistance versus carrier density in Figure 4(d). The HV-Bi and UHV-Bi both present a similar contact resistance value versus carrier density. A detailed statistical study of the device behavior is beyond the scope of this work and will be presented elsewhere.³¹

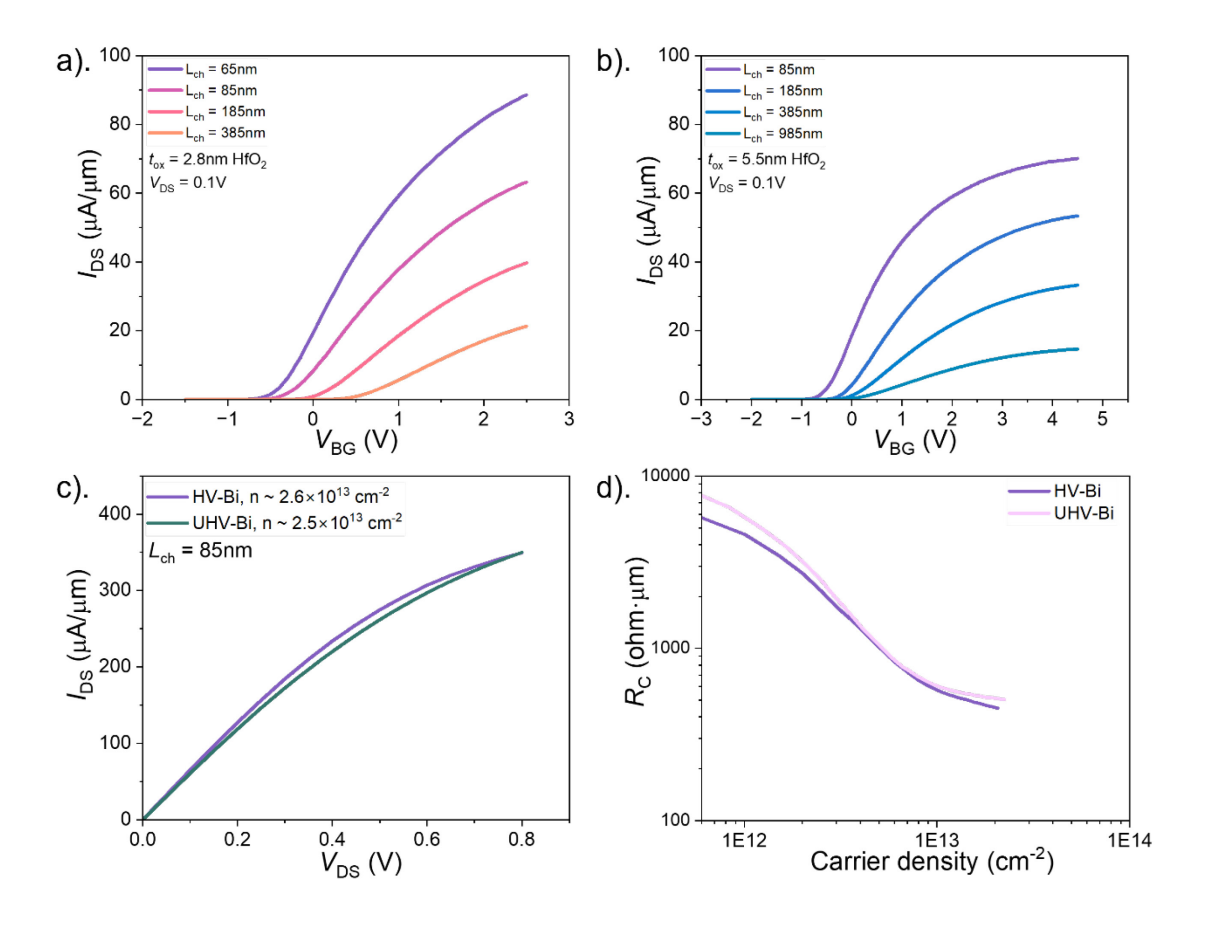


Figure 4 Transfer characteristics and contact resistance of HV-Bi and UHV-Bi ML MoS₂ FETs. (a) Transfer curves of a set of HV-Bi contacted ML MoS₂ FETs with different channel lengths, from 65nm to 385nm. (b) Transfer curves of a set of UHV-Bi contacted ML MoS₂ FETs with different channel lengths, from 85nm to 985nm. (c) Output characteristics of both HV-Bi and UHV-Bi contacted MoS₂ FETs with $L_{ch} \sim 85$ nm. (d) Contact resistance versus carrier density for HV-Bi and UHV-Bi.

Band Alignment Study of Bi/MoS2 System

Determining the E_F of the bulk-MoS₂ substrate relative to the valence band edge involves extrapolating the low binding energy (BE) tail of the valence band spectrum through linear regression while accounting for the background noise level in the XPS spectrum.^{32,33} This approach provides a constant energy difference between core levels and the valence band edge,

making it suitable for studying E_F shifting and band alignment. (See Supporting Information section S3.) Consequently, the valence band edge serves as an indicator of the initial band alignment in a semiconductor, assuming knowledge of the band gap. Shifts in core levels towards lower or higher BE observed during material deposition correspond to equivalent changes of E_F towards the valence band and conduction band, as described in the supporting information. This technique is valuable for determining the $E_{\rm F}$ shifting in metal-semiconductor heterostructures, 8,9,13,26,34,35 as demonstrated throughout this study, and for assessing band alignment in semiconductor heterostructures.

The initial E_F of bulk-MoS₂ shows variations depending on the scanning areas, even if all samples were exfoliated from the same bulk material, as shown in Figure 5. This is because defects of bulk-MoS₂, including vacancies (V_{Mo} , V_{S}), can cause the Fermi level to shift due to the induced electronic mid-gap states. ^{36,37} Afterward metal deposition under UHV and HV conditions, the shifts of the E_F were analyzed. Interestingly, the Fermi level position formed after metal deposition consistently lies just below the conduction band. In the case of Bi contacts on TMD semiconductor materials, as shown in Figure 5, the Fermi level position remains relatively uniform and close to the work function for Bi (ϕ_{WF} = 4.25 eV)³⁸. Even though the previous conventional metal contact reports have highlighted the significant influence of Fermi level pinning due to interfacial properties and reactions, irrespective of work functions, ^{6,8,11,39,40} this observation provides evidence of the strong suppression of MIGS resulting from the *d*-orbital characteristics in the valence band of MoS₂, influenced by the semi-metallic nature of Bi.

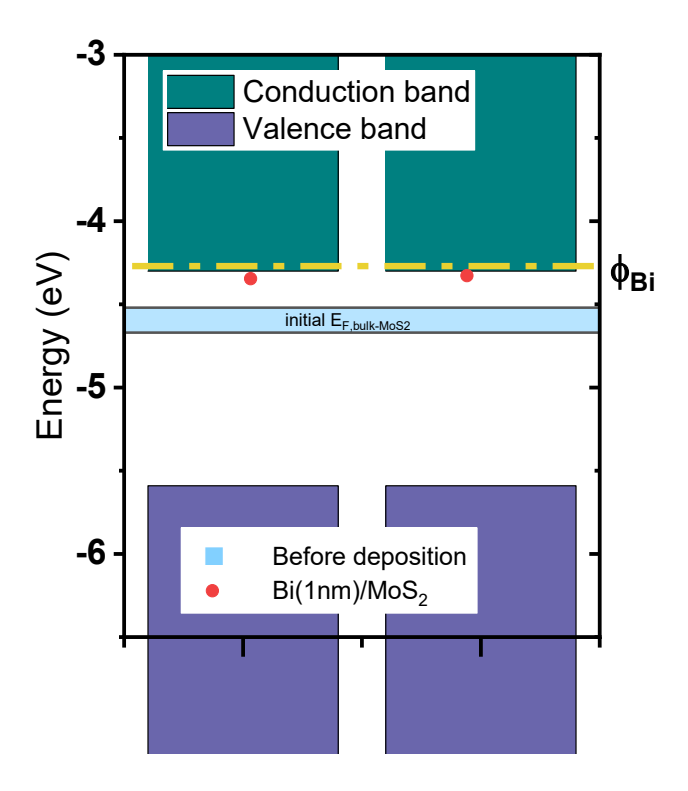


Figure 5 Band alignment of Bi contacts with bulk-MoS₂ before and after Bi deposition under UHV and HV conditions. The E_Fs obtained from the initial valence band maximum and the TMD core level shift after metallization in corresponding conditions. The Bi work function value is denoted by the dash-dotted line in the schematic.

In order to gain a deeper understanding of the E_F and electrical contact properties at the interface between Bi and MoS₂ used in the device fabrication, a sample of 1L-MoS₂ was prepared for STM and STS investigations. (see Supporting Information section S4.) The lattice constants of the measured MoS₂ were determined by STM to be 3.16 Å, (see Supporting Information section S4) aligning with the reported lattice constants of single-layer MoS₂.^{36,41,42} In addition, STS measurements were performed to investigate the electrical properties of the Bi/MoS₂ system. By analyzing the first derivative of the current-voltage (I-V) curve, denoted as dI/dV, it could quantitatively assess the local electron density of states (LDOS) on the surface.^{43,44} Figure S5

shows the different LDOS of each location, but the conduction band minimum is close to the E_F. Additionally, (110) and (111) surface orientations of the Bi are detected. Figure 6 presents STM and STS results for various defects at room temperature. The data acquisitions were conducted at room temperature to elucidate the contact interface properties under actual device operation temperature. The STM image showcases the MoS₂ structure on the Bi (110) surface, with a few defects circled in red. Subsequently, four STS measurements were performed along the red line indicated in Figure 6(a), as shown in Figure 6(b).

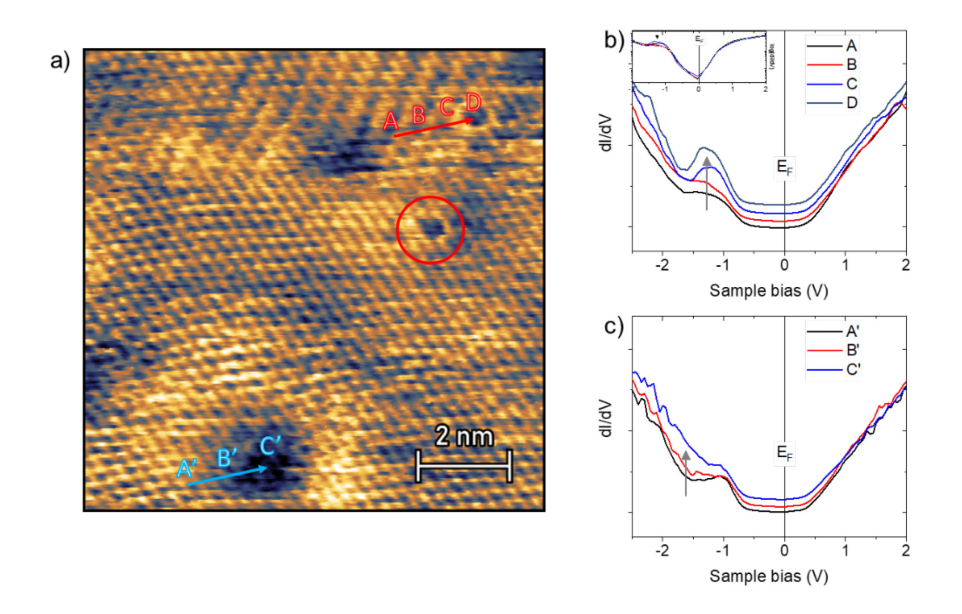


Figure 6 (a) an STM image taken from 1L-MoS₂ on a Bi film (Thickness = 50 nm). (b) STS spectra were taken following the red line in the STM image, and (c) STS spectra were taken following the blue line in the STM image. Image obtained at 0.4 V sample bias, 0.5 nA tunneling current. The inset figure (b) shows the STS spectra in logarithmic.

As the scanning spot approaches a defect on the sample surface, a distinct defect state emerged in the STS spectra at -1.25 V. This defect state corresponds to Molybdenum vacancy (V_{Mo}), an unfilled state formation, as shown in Figure 6(a) under positive sample bias. Figure 6 (b, c) show

that the position of the defect state (indicated by the gray arrow) in the STS agrees with the reported results from low-temperature (77 K) STM measurements and the DFT calculations, which assume 0 K ground state conditions, were close to the VBM.^{37,45–47} Despite the presence of this defect, it appears that the n-type characteristic of Bi/MoS₂ is not significantly influenced. There are no discernible alterations in LDOS formation near the CBM, irrespective of the proximity to the defect. The inset of Figure 6(b) presents the STS in a logarithmic scale for a more apparent observation. The lowest dI/dV value remained constant at -0.05 V without shifting while the p-type defect state appeared.

To summarize, this portion of the study investigated the relationship of surface/interface properties and electrical contact properties of the semi-metallic Bi and MoS₂ interface at room temperature. Valuable insights, by XPS, were gained into E_F shifting and band alignment in semimetal-semiconductor heterostructures. The initial E_F of MoS₂ exhibited variations attributed to defects. After metal deposition under UHV and HV conditions, the E_F is consistently positioned just below the conduction band, indicating the strong suppression of MIGS due to Bi's semi-metallic nature. Further investigation using STM and STS on 1L-MoS₂/Bi revealed consistent E_F locations and electrical properties at the MoS₂/Bi, regardless of defects. Despite the presence of p-type defect states, the n-type characteristic of MoS₂ on Bi remained unaffected, with no discernible alterations in LDOS near the CBM. These findings highlight the robustness of the electrical properties and band alignment at the Bi/MoS₂ interface, which could pave the way for the development of advanced electronic devices.

Thermal stability

The contact interface undergoes significant changes depending on the temperature. Bulk-TMD materials purchased from HQgraphene, are meticulously placed on a titanium sample holder. MoS₂ is securely affixed using stainless steel screws and thoroughly cleansed with nitric acid to prevent contamination during annealing. This cleaning method ensures that the samples can undergo annealing without the risk of contamination from materials such as carbon tape or residues from unclean screws. Thermal stability evaluations were conducted before and after annealing to investigate the interface properties of Bi contacts utilizing an *in-situ* UHV cluster system. The UHV base pressure level was below 3×10⁻¹¹ mbar throughout the process, and the UHV system remained fully isolated once the samples were loaded to inhibit potential contamination. The vacuum conditions during the annealing process were kept below 3×10⁻⁹ mbar. This setup allowed for a detailed examination of the evolution between the metal and TMD at various annealing temperatures.

Figure 7 illustrates the XPS spectra of the Bi/bulk-MoS₂ sample, providing insights into the surface and interface chemistry. Prior to metal deposition, the MoS₂ states were detected in both Mo 3d and S 2p core level spectra, with no observable oxidation features on the MoS₂ surface post-exfoliation (Figures 7(a,b). The interface bonding chemistry between Bi and MoS₂, following Bi deposition, is below the detection limit of XPS, as shown in Figure 1 and Figure 7. Figure 7(c, d) shows the spectrum of carbon and oxygen originating from adventitious carbon.⁵¹ This indicates that these incidental contaminants play an insignificant bonding role at the Bi/TMD interface and remain inert with Bi and MoS₂. It is also noteworthy that weakly bonded adventitious carbon/organics were vaporized at temperatures of 200 °C or higher.

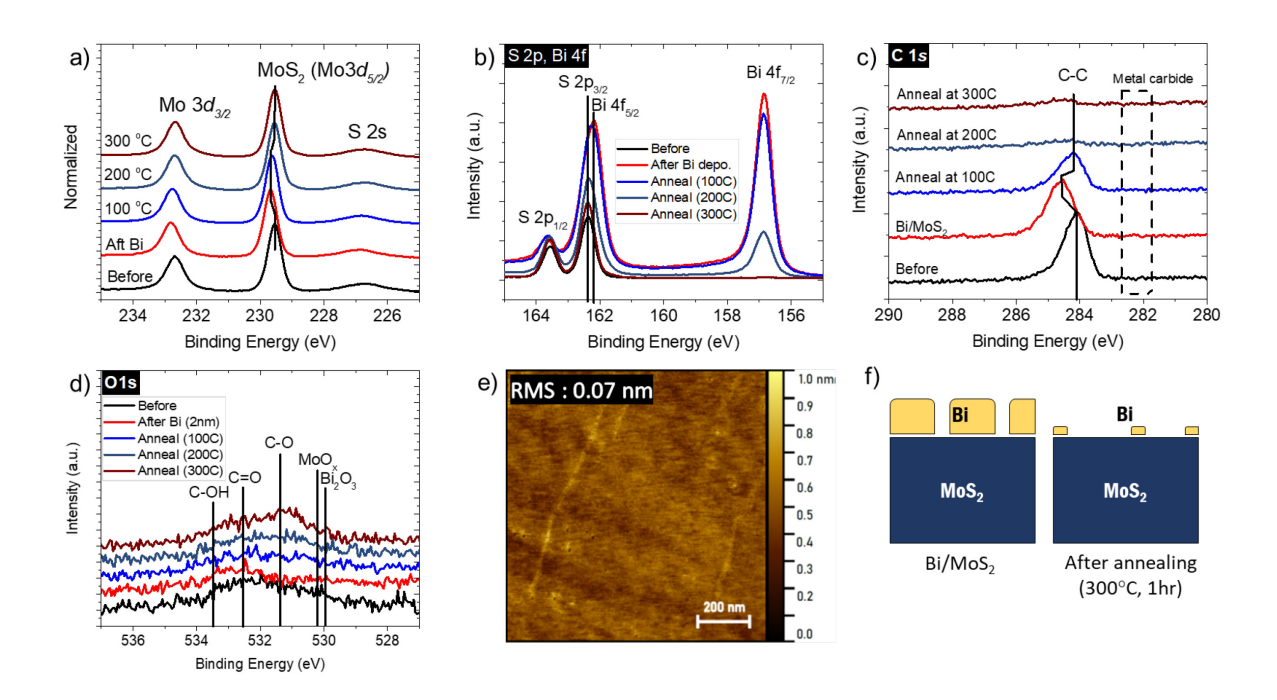


Figure 7 XPS spectra of the bulk-MoS₂ crystal before and after the corresponding fabrication process, (a) Mo 3d, (b) Bi 4f, and S 4p, (c) C 1s, (d) O 1s core levels, (e) AFM image after annealing at 300 °C, and (f) schematic structure of Bi/TMD after Bi deposition (left) and annealing at 300 °C for 1 hour (right).

In Figure 7(b), the Bi 4*f* spectra exhibit a distinct metallic feature, with the intensity diminishing as the annealing temperature increases. Following annealing at 300 °C, the Bi intensity approaches the noise level of XPS spectra, and no detectable reaction products between Bi and MoS₂, such as Bi₂S₃, MoBi_xS_y, or MoS_x, emerge in the XPS spectra. This reduction in intensity can be attributed to the elevated vapor pressure of Bi, which exceeds ~6×10⁻⁹ mbar at 300 °C, causing the desorption and vaporization of Bi under the UHV conditions.^{52,53} The rapid change in chamber pressure observed during annealing further supports the Bi evaporation. Although the possibility of Bi diffusion into the MoS₂ substrate cannot be entirely ruled out, the evidence strongly suggests that evaporation is the primary factor contributing to the disappearance of Bi in this study. This result

demonstrates the need for capping (encapsulating) the Bi contact for better thermal stability in device fabrication. As noted previously, the devices typically incorporate a Au capping layer accordingly.³¹

The surface morphology of Bi/MoS₂ systems has been studied by room temperature AFM after 300 °C anneal under UHV. In the preceding sections, we established that Bi tends to form islands on all MoS₂ due to their weak interaction. After 300 °C anneal in UHV, Bi islands disappeared, and an atomically flat surface was observed, measured as 0.07 nm of RMS roughness. This result is congruent with the observation from XPS analysis that there is no detectable reaction or deformation of MoS₂ during Bi sublimation. These results suggest that the persistence of weak vdW bonding at the Bi/MoS₂ interface is present regardless of thermal treatment; Figure 7(f) is the schematic image before and after the annealing process. It is also clear that, in the context of device fabrication thermal budgets, contacts incorporating Bi may be problematic if not capped to inhibit desorption/vaporization.^{22,31}

Conclusions

In conclusion, this comprehensive study delves into the interface properties and thermal stability of Bi contacts on MoS₂, with device measurements indicating minimal differences between UHV and HV deposition conditions, supported by detailed characterization showing consistent chemical states and interface quality under both conditions. The key findings include the effective suppression of DIGS without MIGS at the interface of Bi/MoS₂, evidenced by E_F aligning below the conduction band following Bi deposition. STM and STS analysis reveals that E_F is unchanged despite the presence of defects. The subsequent study extends this work to examining the thermal stability of the Bi contact interface up to 300 °C. A thermally stable interface was observed while

Bi was sublimated and vaporized under UHV conditions. This study offers a comprehensive and fundamental understanding of the interplay between processing conditions, interface chemistry, and electrical contact properties, providing valuable insights that can be harnessed in optimizing device design and performance for practical applications. It offers a pathway to achieve optimal device performance consistently, particularly in the context of semi-metallic contacts on TMD systems.

Experimental Methods

Bulk-MoS₂ sample preparation

Bulk-MoS₂, purchased from HQgraphene,⁵⁰ is prepared by locating on a sample holder, a metal plate made of titanium, and the top layers of MoS₂ were exfoliated by the scotch tape just before loading the sample into the chamber, then the pressure reached a HV condition in less than 1 min. It was noted that these bulk-MoS₂ materials can provide high-quality crystallinity compared to the grown few layers of MoS₂, which therefore provides a fundamental understanding of the interface chemistry in an ideal situation.

1L-MoS₂ sample preparation

For the contact resistance and interface characteristics of monolayer MoS₂ (1L-MoS₂), chemical vapor deposition (CVD)-grown 1L-MoS₂ was purchased from 2dsemiconductors.⁵⁴ The CVD-grown 1L-MoS₂ was transferred to HfO₂ substrates using polymethyl methacrylate (PMMA). Samples for device and interface characterization were prepared accordingly. The metal (contact) deposition was performed under UHV and HV conditions by the different e-beam evaporators at UT-Dallas. The contact chemical characteristics between the metal and MoS₂ were examined using monochromatic x-ray photoelectron spectroscopy (XPS), atomic force microscopy (AFM),

scanning tunneling microscopy (STM), and subsequent field effect transistor (FET) measurements at Purdue.

1L-MoS₂ FET fabrication and measurement

1L-MoS₂ was wet transferred onto the local bottom gate substrates at Purdue.²⁹ The local bottom gate substrates consist of a stack of Cr/Au (2/13nm) as gate metal, 5.5nm HfO₂ as a dielectric layer grown by ALD. After the wet transfer process, the sample is annealed at a pressure of ~7×10⁻⁸ mbar at 200 °C for 2 hours. Optical microscopy is used to identify flakes located on local bottom gates, and the sample is spin-coated with photoresist PMMA and baked at 180 °C for 5 mins. Next, source/drain contacts are patterned by a JEOL JBX-8100FS E-Beam Writer system at Purdue and developed in an IPA/DI solution. This pattern process is then followed by e-beam evaporation of 20nm Bi and 50nm Au as a contact metal structure, with the Au layer utilized as a capping layer to protect the Bi from spurious oxidation. These contact metal deposition processes were done under UHV or HV conditions at UT-Dallas as described below: Bi/Au (20/50nm) contacts were deposited sequentially in the respective vacuum chamber.^{55,56} Next, the sample undergoes a lift-off process at Purdue for subsequent electrical characterization.

A Lake Shore CPX-VF probe station and Agilent 4155C Semiconductor Parameter Analyzer are used to perform the electrical characterization at room temperature in high vacuum ($\approx 10^{-6}$ mbar). Standard DC sweeps are used in the electrical measurements for all devices. All devices are measured as fabricated at Purdue.

Metal deposition under UHV and HV conditions.

A titanium sample plate (4-inch diameter) was loaded into the analytical chamber for *in-situ* XPS characterization to study the surface before metal deposition. Samples (10mm × 10mm) with the interfaces of interest were mounted on the plate. Bismuth films of approximately 1 nm

thickness were deposited on both bulk-MoS₂ crystal and 1L-MoS₂ film samples for XPS measurements. The thickness of the deposited Bi was monitored using a QCM, which was regularly calibrated to ensure accuracy by measuring the thickness on a flat Si substrate using AFM and a step profilometer. The deposition was carried out using an *ex-situ* high-vacuum (HV) e-beam evaporator (base pressure ~4×10⁻⁶ mbar) and an *in-situ* ultra-high-vacuum (UHV) e-beam evaporator (base pressure ~2×10⁻¹¹ mbar). For the HV deposition, the sample after the metal deposition was exposed to air for 5 minutes until reaching a HV (~1×10⁻⁶ mbar) environment in the load lock for subsequent XPS characterizations. In the case of UHV (HV) metal deposition, the process involved using an acceleration voltage of 9 (9) kV, an e-beam current of approximately 39 (45) mA, resulting in a deposition rate of 0.2 (0.2) Å per second for Bi. The substrate was consistently maintained at room temperature throughout the deposition process, and the temperature was continuously monitored using a thermocouple. For the films deposited under UHV, the associated samples were transferred under UHV conditions (~2×10⁻¹¹ mbar) to the analytical chamber through a transfer tube, a backbone interconnecting each chamber.^{42,55,57}

For device contacts, the deposition process, including the deposition rate, base pressure, and acceleration voltage, was maintained identical to that of the XPS-measured sample. The thicker (20nm) Bi layers were deposited e-beam evaporation followed by 50 nm Au for capping and contact purposes in the same chamber.

Monochromatic XPS

XPS characterization was performed using a monochromatic Al Kα X-ray source with an energy of 1486.7 eV and an Omicron EA125 hemispherical analyzer.⁵⁸ Standard ASTM procedures were followed to ensure accurate calibration of the EA125 energy analyzer.⁵⁹ This involved attaching sputter-cleaned Au, Ag, and Cu foils to the manipulator for convenient calibration as needed.⁵⁹

XPS core level scans were carried out both before and after the deposition of metal contacts, utilizing a take-off angle of 45° and a resolution of 0.05 eV. The AAnalyzer peak fitting software was employed to analyze all obtained features, ensuring precise spectral fitting.⁶⁰ In this process, uniformity was maintained across all spectra parameters for each feature. This encompassed the background function, peak shape, and peak width, contributing to the accuracy of the analysis.

Scanning Tunneling Microscopy/Spectroscopy.

Samples were prepared using an exfoliation process to facilitate STM/STS and XPS measurements as described in the Supporting Information, section S4. The STM images were acquired using an Omicron VT-STM/AFM system with the constant current mode at room temperature.⁴² Each STS spectrum is averaged from at least 15 repetitions to enhance the signal-to-noise ratio. The STM images were processed using Gwyddion software.⁶¹

ASSOCIATED CONTENT

Supporting Information

Supporting Information is available free of charge.

Interface Chemistry of Bi/1L-MoS₂; Air-stability of UHV-Bi/MoS₂; The FWHM and the binding energies of Bi and MoS₂(1L-, Bulk, Air-exposure) systems; Extraction of valence band maximum of MoS₂ and Fermi level shift; Sample preparation and STM/STS results of 1L-MoS₂/Bi sample; (PDF)

AUTHOR INFORMATION

Corresponding Author

Robert M. Wallace - Department of Materials Science and Engineering, The University of Texas at Dallas, Richardson, TX 75080, United States of America; orcid.org/0000-0001-5566-4806; E-mail: rmwallace@utdallas.edu

ACKNOWLEDGMENT

This work was supported in part by NEWLIMITS, a center in nCORE, a Semiconductor Research Corporation (SRC) program sponsored by NIST through award number 70NANB17H041, the National Science Foundation through award DMR-2002741, and the Erik Jonsson Distinguished Chair.

REFERENCES

- (1) Radisavljevic, B.; Radenovic, A.; Brivio, J.; Giacometti, V.; Kis, A. Single-Layer MoS₂ Transistors. *Nature Nanotech* **2011**, *6* (3), 147–150. https://doi.org/10.1038/nnano.2010.279.
- (2) Kim, S.; Konar, A.; Hwang, W.-S.; Lee, J. H.; Lee, J.; Yang, J.; Jung, C.; Kim, H.; Yoo, J.-B.; Choi, J.-Y.; Jin, Y. W.; Lee, S. Y.; Jena, D.; Choi, W.; Kim, K. High-Mobility and Low-Power Thin-Film Transistors Based on Multilayer MoS₂ Crystals. *Nat Commun* **2012**, *3* (1), 1011. https://doi.org/10.1038/ncomms2018.
- (3) Choi, W.; Cho, M. Y.; Konar, A.; Lee, J. H.; Cha, G.-B.; Hong, S. C.; Kim, S.; Kim, J.; Jena, D.; Joo, J.; Kim, S. High-Detectivity Multilayer MoS₂ Phototransistors with Spectral Response from Ultraviolet to Infrared. *Advanced Materials* **2012**, *24* (43), 5832–5836. https://doi.org/10.1002/adma.201201909.

- (4) Smyth, C. M.; Walsh, L. A.; Bolshakov, P.; Catalano, M.; Schmidt, M.; Sheehan, B.; Addou, R.; Wang, L.; Kim, J.; Kim, M. J.; Young, C. D.; Hinkle, C. L.; Wallace, R. M. Engineering the Interface Chemistry for Scandium Electron Contacts in WSe₂ Transistors and Diodes. *2D Mater.* **2019**, *6* (4), 045020. https://doi.org/10.1088/2053-1583/ab2c44.
- (5) McDonnell, S. J.; Wallace, R. M. Atomically-Thin Layered Films for Device Applications Based upon 2D TMDC Materials. *Thin Solid Films* **2016**, *616*, 482–501. https://doi.org/10.1016/j.tsf.2016.08.068.
- (6) Gong, C.; Colombo, L.; Wallace, R. M.; Cho, K. The Unusual Mechanism of Partial Fermi Level Pinning at Metal–MoS₂ Interfaces. *Nano Lett.* **2014**, *14* (4), 1714–1720. https://doi.org/10.1021/nl403465v.
- (7) Jang, J.; Ra, H.-S.; Ahn, J.; Kim, T. W.; Song, S. H.; Park, S.; Taniguch, T.; Watanabe, K.; Lee, K.; Hwang, D. K. Fermi-Level Pinning-Free WSe₂ Transistors via 2D Van Der Waals Metal Contacts and Their Circuits. *Advanced Materials* **2022**, *34* (19), 2109899. https://doi.org/10.1002/adma.202109899.
- (8) Smyth, C. M.; Addou, R.; Hinkle, C. L.; Wallace, R. M. Origins of Fermi-Level Pinning between Molybdenum Dichalcogenides (MoSe₂, MoTe₂) and Bulk Metal Contacts: Interface Chemistry and Band Alignment. *J. Phys. Chem. C* **2019**, *123* (39), 23919–23930. https://doi.org/10.1021/acs.jpcc.9b04355.
- (9) Smyth, C. M.; Addou, R.; Hinkle, C. L.; Wallace, R. M. Origins of Fermi Level Pinning between Tungsten Dichalcogenides (WS₂, WTe₂) and Bulk Metal Contacts: Interface Chemistry and Band Alignment. *J. Phys. Chem. C* **2020**, *124* (27), 14550–14563. https://doi.org/10.1021/acs.jpcc.0c01646.

- (10) Schottky, W. Über den Mechanismus der Ionenbewegung in festen Elektrolyten. *Zeitschrift für Physikalische Chemie* **1935**, *29B* (1), 335–355. https://doi.org/10.1515/zpch-1935-2934.
- (11) Kim, C.; Moon, I.; Lee, D.; Choi, M. S.; Ahmed, F.; Nam, S.; Cho, Y.; Shin, H.-J.; Park, S.; Yoo, W. J. Fermi Level Pinning at Electrical Metal Contacts of Monolayer Molybdenum Dichalcogenides. *ACS Nano* **2017**, *11* (2), 1588–1596. https://doi.org/10.1021/acsnano.6b07159.
- (12) McDonnell, S.; Addou, R.; Buie, C.; Wallace, R. M.; Hinkle, C. L. Defect-Dominated Doping and Contact Resistance in MoS₂. *ACS Nano* **2014**, 8 (3), 2880–2888. https://doi.org/10.1021/nn500044q.
- (13) McDonnell, S.; Smyth, C.; Hinkle, C. L.; Wallace, R. M. MoS₂ –Titanium Contact Interface Reactions. *ACS Appl. Mater. Interfaces* **2016**, 8 (12), 8289–8294. https://doi.org/10.1021/acsami.6b00275.
- (14) Bolshakov, P.; Smyth, C. M.; Khosravi, A.; Zhao, P.; Hurley, P. K.; Hinkle, C. L.; Wallace, R. M.; Young, C. D. Contact Engineering for Dual-Gate MoS₂ Transistors Using O₂ Plasma Exposure. *ACS Appl. Electron. Mater.* **2019**, *I* (2), 210–219. https://doi.org/10.1021/acsaelm.8b00059.
- (15) Tersoff, J. Schottky Barrier Heights and the Continuum of Gap States. *Phys. Rev. Lett.* **1984**, *52* (6), 465–468. https://doi.org/10.1103/PhysRevLett.52.465.
- (16) Shen, P.-C.; Su, C.; Lin, Y.; Chou, A.-S.; Cheng, C.-C.; Park, J.-H.; Chiu, M.-H.; Lu, A.-Y.; Tang, H.-L.; Tavakoli, M. M.; Pitner, G.; Ji, X.; Cai, Z.; Mao, N.; Wang, J.; Tung, V.; Li, J.; Bokor, J.; Zettl, A.; Wu, C.-I.; Palacios, T.; Li, L.-J.; Kong, J. Ultralow Contact Resistance

between Semimetal and Monolayer Semiconductors. *Nature* **2021**, *593* (7858), 211–217. https://doi.org/10.1038/s41586-021-03472-9.

- (17) Bampoulis, P.; van Bremen, R.; Yao, Q.; Poelsema, B.; Zandvliet, H. J. W.; Sotthewes, K. Defect Dominated Charge Transport and Fermi Level Pinning in MoS₂/Metal Contacts. *ACS Appl. Mater. Interfaces* **2017**, *9* (22), 19278–19286. https://doi.org/10.1021/acsami.7b02739.
- (18) Chou, A.-S.; Cheng, C.-C.; Liew, S.-L.; Ho, P.-H.; Wang, S.-Y.; Chang, Y.-C.; Chang, C.-K.; Su, Y.-C.; Huang, Z.-D.; Fu, F.-Y.; Hsu, C.-F.; Chung, Y.-Y.; Chang, W.-H.; Li, L.-J.; Wu, C.-I. High On-State Current in Chemical Vapor Deposited Monolayer MoS₂ nFETs With Sn Ohmic Contacts. *IEEE Electron Device Letters* **2021**, *42* (2), 272–275. https://doi.org/10.1109/LED.2020.3048371.
- (19) Dorow, C.; O'Brien, K.; Naylor, C. H.; Lee, S.; Penumatcha, A.; Hsiao, A.; Tronic, T.; Christenson, M.; Maxey, K.; Zhu, H.; Oni, A.; Alaan, U.; Gosavi, T.; Gupta, A. S.; Bristol, R.; Clendenning, S.; Metz, M.; Avci, U. Advancing Monolayer 2-D nMOS and pMOS Transistor Integration From Growth to Van Der Waals Interface Engineering for Ultimate CMOS Scaling. *IEEE Transactions on Electron Devices* **2021**, *68* (12), 6592–6598. https://doi.org/10.1109/TED.2021.3118659.
- (20) Haynes, W. M.; Lide, D. R.; Bruno, T. J. CRC Handbook of Chemistry and Physics (2016-2017)-CRC Press (2016), 2016.
- (21) International Roadmap for Devices and Systems (IRDSTM) 2022 Edition IEEE IRDSTM. https://irds.ieee.org/editions/2022 (accessed 2023-07-05).

- (22) Schmitz, J. Low Temperature Thin Films for Next-Generation Microelectronics (Invited). Surface and Coatings Technology 2018, 343, 83–88. https://doi.org/10.1016/j.surfcoat.2017.11.013.
- (23) Justin Gorham. NIST X-Ray Photoelectron Spectroscopy Database SRD 20, 2012. https://doi.org/10.18434/T4T88K.
- (24) Park, S.; Kim, S. Y.; Choi, Y.; Kim, M.; Shin, H.; Kim, J.; Choi, W. Interface Properties of Atomic-Layer-Deposited Al₂O₃ Thin Films on Ultraviolet/Ozone-Treated Multilayer MoS₂ Crystals. *ACS Appl. Mater. Interfaces* **2016**, 8 (18), 11189–11193. https://doi.org/10.1021/acsami.6b01568.
- (25) English, C. D.; Shine, G.; Dorgan, V. E.; Saraswat, K. C.; Pop, E. Improved Contacts to MoS₂ Transistors by Ultra-High Vacuum Metal Deposition. *Nano Lett.* **2016**, *16* (6), 3824–3830. https://doi.org/10.1021/acs.nanolett.6b01309.
- (26) Smyth, C. M.; Addou, R.; McDonnell, S.; Hinkle, C. L.; Wallace, R. M. Contact Metal–MoS₂ Interfacial Reactions and Potential Implications on MoS₂ -Based Device Performance. *J. Phys. Chem. C* **2016**, *120* (27), 14719–14729. https://doi.org/10.1021/acs.jpcc.6b04473.
- (27) Freedy, K. M.; Zhu, T.; Olson, D. H.; Litwin, P. M.; Hopkins, P. E.; Zebarjadi, M.; McDonnell, S. J. Interface Chemistry and Thermoelectric Characterization of Ti and TiO_x Contacts to MBE-Grown WSe₂. *2D Mater.* **2020**, *7* (4), 045033. https://doi.org/10.1088/2053-1583/ab834b.
- (28) Blair, J. C.; Ghate, P. B. Effect of Vacuum Ambience on Al–Si Contacts. *Journal of Vacuum Science and Technology* **1977**, *14* (1), 79–84. https://doi.org/10.1116/1.569178.

- (29) Sun, Z.; Chen, C.; Robinson, J. A.; Chen, Z.; Appenzeller, J. A Mobility Study of Monolayer MoS₂ on Low-κ/High-κ Dielectrics. In *2023 Device Research Conference (DRC)*; IEEE: Santa Barbara, CA, USA, 2023; pp 1–2. https://doi.org/10.1109/DRC58590.2023.10258241.
- (30) Berger, H. H. Models for Contacts to Planar Devices. *Solid-State Electronics* **1972**, *15* (2), 145–158. https://doi.org/10.1016/0038-1101(72)90048-2.
- (31) Sun, Z.; Kim, S. Y.; Cai, J.; Shen, J.; Lan, H.-Y.; Tan, Y.; Wang, X.; Wang, H.; Shen, C.; Chen, Z.; Wallace, R. M.; Appenzeller, J. Ultralow Contact Resistance on Monolayer MoS2 FETs Induced by Contact Interface Engineering. *ACS Nano* (2024); https://doi.org/10.1021/acsnano.4c07267
- (32) Kraut, E. A.; Grant, R. W.; Waldrop, J. R.; Kowalczyk, S. P. Semiconductor Core-Level to Valence-Band Maximum Binding-Energy Differences: Precise Determination by x-Ray Photoelectron Spectroscopy. *Phys. Rev. B* **1983**, *28* (4), 1965–1977. https://doi.org/10.1103/PhysRevB.28.1965.
- (33) Dong, H.; Gong, C.; Addou, R.; McDonnell, S.; Azcatl, A.; Qin, X.; Wang, W.; Wang, W.; Hinkle, C. L.; Wallace, R. M. Schottky Barrier Height of Pd/MoS₂ Contact by Large Area Photoemission Spectroscopy. *ACS Appl. Mater. Interfaces* **2017**, *9* (44), 38977–38983. https://doi.org/10.1021/acsami.7b10974.
- (34) Wang, X.; Kim, S. Y.; Wallace, R. M. Interface Chemistry and Band Alignment Study of Ni and Ag Contacts on MoS₂. *ACS Appl. Mater. Interfaces* **2021**, *13* (13), 15802–15810. https://doi.org/10.1021/acsami.0c22476.

- (35) Wang, X.; Hu, Y.; Kim, S. Y.; Addou, R.; Cho, K.; Wallace, R. M. Origins of Fermi Level Pinning for Ni and Ag Metal Contacts on Tungsten Dichalcogenides. *ACS Nano* **2023**. https://doi.org/10.1021/acsnano.3c06494.
- (36) Vancsó, P.; Magda, G. Z.; Pető, J.; Noh, J.-Y.; Kim, Y.-S.; Hwang, C.; Biró, L. P.; Tapasztó, L. The Intrinsic Defect Structure of Exfoliated MoS2 Single Layers Revealed by Scanning Tunneling Microscopy. *Sci Rep* **2016**, *6* (1), 29726. https://doi.org/10.1038/srep29726.
- (37) Kc, S.; Longo, R. C.; Addou, R.; Wallace, R. M.; Cho, K. Impact of Intrinsic Atomic Defects on the Electronic Structure of MoS₂ Monolayers. *Nanotechnology* **2014**, *25* (37), 375703. https://doi.org/10.1088/0957-4484/25/37/375703.
- (38) Springer Handbook of Electronic and Photonic Materials; Kasap, S., Capper, P., Eds.; Springer Handbooks; Springer International Publishing: Cham, 2017. https://doi.org/10.1007/978-3-319-48933-9.
- (39) Wang, X.; Kim, S. Y.; Wallace, R. M. Interface Chemistry and Band Alignment Study of Ni and Ag Contacts on MoS₂. *ACS Appl. Mater. Interfaces* **2021**, *13* (13), 15802–15810. https://doi.org/10.1021/acsami.0c22476.
- (40) Liu, X.; Choi, M. S.; Hwang, E.; Yoo, W. J.; Sun, J. Fermi Level Pinning Dependent 2D Semiconductor Devices: Challenges and Prospects. *Advanced Materials* **2022**, *34* (15), 2108425. https://doi.org/10.1002/adma.202108425.
- (41) Trainer, D. J.; Putilov, A. V.; Di Giorgio, C.; Saari, T.; Wang, B.; Wolak, M.; Chandrasena, R. U.; Lane, C.; Chang, T.-R.; Jeng, H.-T.; Lin, H.; Kronast, F.; Gray, A. X.; Xi, X.; Nieminen, J.;

- Bansil, A.; Iavarone, M. Inter-Layer Coupling Induced Valence Band Edge Shift in Mono- to Few-Layer MoS2. *Sci Rep* **2017**, *7* (1), 40559. https://doi.org/10.1038/srep40559.
- (42) Addou, R.; Colombo, L.; Wallace, R. M. Surface Defects on Natural MoS₂. *ACS Appl. Mater. Interfaces* **2015**, *7* (22), 11921–11929. https://doi.org/10.1021/acsami.5b01778.
- (43) Stroscio, J. A.; Feenstra, R. M.; Fein, A. P. Electronic Structure of the Si(111)2×1 Surface by Scanning-Tunneling Microscopy. *Phys. Rev. Lett.* **1986**, *57* (20), 2579–2582. https://doi.org/10.1103/PhysRevLett.57.2579.
- (44) Feenstra, R. M. A Prospective: Quantitative Scanning Tunneling Spectroscopy of Semiconductor Surfaces. *Surface Science* **2009**, *603* (18), 2841–2844. https://doi.org/10.1016/j.susc.2009.08.002.
- (45) Trainer, D. J.; Nieminen, J.; Bobba, F.; Wang, B.; Xi, X.; Bansil, A.; Iavarone, M. Visualization of Defect Induced In-Gap States in Monolayer MoS₂. *npj 2D Mater Appl* **2022**, *6* (1), 1–7. https://doi.org/10.1038/s41699-022-00286-9.
- (46) Salehi, S.; Saffarzadeh, A. Atomic Defect States in Monolayers of MoS₂ and WS₂. *Surface Science* **2016**, *651*, 215–221. https://doi.org/10.1016/j.susc.2016.05.003.
- (47) Qiu, X.; Wang, Y.; Jiang, Y. First-Principles Study of Vacancy Defects at Interfaces between Monolayer MoS₂ and Au. *RSC Adv.* **2020**, *10* (48), 28725–28730. https://doi.org/10.1039/D0RA04833J.
- (48) Smyth, C. M.; Walsh, L. A.; Bolshakov, P.; Catalano, M.; Addou, R.; Wang, L.; Kim, J.; Kim, M. J.; Young, C. D.; Hinkle, C. L.; Wallace, R. M. Engineering the Palladium-WSe₂

Interface Chemistry for Field Effect Transistors with High-Performance Hole Contacts. *ACS Appl. Nano Mater.* **2019**, *2* (1), 75–88. https://doi.org/10.1021/acsanm.8b01708.

- (49) Freedy, K. M.; Zhang, H.; Litwin, P. M.; Bendersky, L. A.; Davydov, A. V.; McDonnell, S. Thermal Stability of Titanium Contacts to MoS₂. *ACS Appl. Mater. Interfaces* **2019**, *11* (38), 35389–35393. https://doi.org/10.1021/acsami.9b08829.
- (50) HQ graphene is a manufacturer of high quality 2D crystals. https://hqgraphene.com/index.php (accessed 2023-08-12).
- (51) Greczynski, G.; Hultman, L. The Same Chemical State of Carbon Gives Rise to Two Peaks in X-Ray Photoelectron Spectroscopy. *Sci Rep* **2021**, *11* (1), 11195. https://doi.org/10.1038/s41598-021-90780-9.
- (52) Fischer, A. K. Vapor Pressure of Bismuth. *The Journal of Chemical Physics* **1966**, *45* (1), 375–377. https://doi.org/10.1063/1.1727337.
- (53) Aldred, A. T.; Pratt, J. N. Vapor Pressure of Liquid Bismuth. *The Journal of Chemical Physics* **1963**, *38* (5), 1085–1087. https://doi.org/10.1063/1.1733806.
- (54) 2D Semiconductors | World's Largest Quantum and 2D Materials Manufacturer. https://2dsemiconductors.com/ (accessed 2024-05-02).
- (55) Wallace, R. M. In-Situ Studies of Interfacial Bonding of High-k Dielectrics for CMOS Beyond 22nm. *ECS Trans.* **2008**, *16* (5), 255–271. https://doi.org/10.1149/1.2981608.
- (56) Cleanroom Tools Cleanroom Research Laboratory | The University of Texas at Dallas. https://cleanroom.utdallas.edu/tools/ (accessed 2024-02-03).

- (57) Wallace, R. M. In-Situ Studies on 2D Materials. *ECS Trans.* **2014**, *64* (9), 109. https://doi.org/10.1149/06409.0109ecst.
- (58) Schweppe, J.; Deslattes, R. D.; Powellb, C. J. Accurate Measurement of Mg and Al Kα_{1,2} X-Ray Energy Profiles. *J. Electron Spectrosc. Relat. Phenom.* **1994**.
- (59) E42 Committee. *Standard Practice for Calibration of the Electron Binding-Energy Scale of an X-Ray Photoelectron Spectrometer*; ASTM International. https://doi.org/10.1520/E2108-16.
 - (60) XPS OASIS. https://xpsoasis.org/ (accessed 2024-04-23).
- (61) Nečas, D.; Klapetek, P. Gwyddion: An Open-Source Software for SPM Data Analysis. *Open Physics* **2012**, *10* (1), 181–188. https://doi.org/10.2478/s11534-011-0096-2.